Defect-free, few-atomic-layer thin ZnO nanosheets with superior excitonic properties for optoelectronic devices

Mandeep Singh[1,ǂ], Muhammad Zakria[2,ǂ], Amandeep Singh Pannu[3], Prashant Sonar[3,*], Christopher Smith[2], Sanje Mahasivam[1], Rajesh Ramanathan[1], Kevin Tran[4], Sherif Tawfik[5], Billy James Murdoch[6], Edwin Lawrence Harrop Mayes[6], Michelle J. S. Spencer[4], Matthew R. Phillips[2], Vipul Bansal[1,*], Cuong Ton-That[2,*]

[1] *Ian Potter NanoBioSensing Facility, NanoBiotechnology Research laboratory, School of Science, RMIT University, Melbourne VIC 3000, Australia*

[2] *School of Mathematical and Physical Sciences, University of Technology Sydney, Ultimo, NSW 2007, Australia*

[3] *School of Chemistry, Physics, and Mechanical Engineering, Queensland University of Technology, Brisbane, QLD 4000, Australia*

[4] *ARC Centre of Excellence in Future Low-Energy Electronics Technologies, School of Science, RMIT University, Melbourne, VIC 3001, Australia*

[5] *ARC Centre of Excellence in Exciton Science, School of Science, RMIT University, Melbourne, VIC 3000, Australia*

[6] *RMIT Microscopy and Microanalysis Facility, STEM College, RMIT University, Melbourne, VIC 3001, Australia*

* Corresponding authors: vipul.bansal@rmit.edu.au; sonar.prashant@qut.edu.au; cuong.ton-that@uts.edu.au

ǂ Authors contributed equally to this work.

ABSTRACT

Two-dimensional (2D) wide bandgap materials are gaining significant interest for next-generation optoelectronic devices. However, fabricating electronic-grade 2D nanosheets from non-van der Waals (n-vdW) oxide semiconductors poses a great challenge due to their stronger interlayer coupling compared with vdW crystals. This strong coupling typically introduces defects during exfoliation, impairing their optoelectronic properties. Herein, we report the liquid-phase exfoliation of few-atomic-layer thin, defect-free, free-standing ZnO nanosheets. These micron-

sized, ultrathin ZnO structures exhibit three different orientations aligned along both the polar *c*-plane as well as the non-polar *a*- and *m*-planes. The superior crystalline quality of ZnO nanosheets is validated through comprehensive characterization techniques. This result is supported by density functional theory (DFT) calculations, which reveals that the formation of oxygen vacancies is energetically less favourable in 2D ZnO and that the *c*-plane loses its polarity upon exfoliation. Unlike bulk ZnO, which is typically dominated by defect-induced emission, the exfoliated nanosheets exhibit a strong, ambient-stable excitonic UV emission. We further demonstrate the utility of solution-processing of ZnO nanosheets by their hybrid integration with organic components to produce stable light emitting devices (LEDs) for display applications.

KEYWORDS: non-van der Waals 2D materials; liquid-phase exfoliation; nanosheets; quantum confinement; excitons; light emitting diodes

The discovery of single-atomic layer graphene and few-layer transition metal dichalcogenides has led to a surge of interest in other anisotropic vdW crystals characterized by strong in-plane bonds and weaker inter-layer interaction.[1-4] Success with a suite of 2D semiconducting layers of large bandgap vdW materials (such as BN, MoO_3, HfO_2 and $SrTiO_3$)[5-8], and narrow bandgap vdW semiconductors (such as MoS_2, WSe_2 and black phosphorus)[9-11] with unique properties has provided promising platforms for future nano-devices. Liquid phase exfoliation has recently been successfully applied to a limited number of n-vdW semiconductors that lack a layered structure, and the list of such 2D n-vdW materials is rapidly expanding. [4, 12-14] Interest in the realization of a wide range of vdW and n-vdW crystals is stimulated by the possibility of forming lateral heterojunctions for use in emerging electronics, such as of valleytronics,[15] ultrasensitive photodetectors,[16] flexible transistors,[17] memory and spintronic devices.[18]

ZnO is one of the most widely studied wide bandgap materials due to its unique optical, electrical, and mechanical properties. These include highly stable excitons due to large exciton binding energy (60 meV), small electron effective mass, efficient luminescence, high transparency in the visible spectrum, and easily tunable n-type conductivity.[19, 20] These distinct properties have led to extensive applications of ZnO in photonics, piezotronics, optoelectronics and sensor technologies.[21] However, bulk ZnO is known for its susceptibility to a high concentration of defects, particularly oxygen and zinc vacancies (V_O and V_{Zn}), which have a pronounced influence on its electrical and optical properties.[22-24] The possibility of exfoliating ZnO into ultrathin layers presents several exciting opportunities. Firstly, high-quality 2D oxide materials enables innovative device architectures and additional functionalities.[25, 26] Secondly, from a fundamental perspective, realizing the exfoliation of defect-free ZnO nanosheets from the bulk material is crucial for their widespread use in hybrid 2D heterostructures. While layered materials can be easily exfoliated by breaking weak vdW forces, the cleavage of covalently bonded n-vdW systems imposes a significant energy cost, often leading to the introduction of defects in 2D systems. In this context, ZnO has an interesting crystal structure that lies between a vdW and a covalently bonded system, offering the prospect to produce a defect-free material through exfoliation. A defect-free 2D ZnO system is highly desirable for efficient optoelectronic devices.

Herein, we report the successful liquid phase exfoliation of ZnO into high-quality, electronic-grade, few-monolayer-thin 2D nanosheets with lateral dimensions of several micrometers. While bottom-up approaches can produce 2D ZnO, the material obtained through these methods is preferentially oriented along the *c*-plane and often contains large concentrations of defects.[27, 28] Additionally, bottom-up approaches, such as metal-organic chemical vapor deposition (MOCVD), have been attempted to prepare free-standing ZnO films, but these films exhibit a thickness

exceeding 300 nm and lack defined orientation.[29] The top-down exfoliation method employed here offers key advantages over existing methods. Firstly, it allows the production of superior quality ultrathin 2D crystals, unlike the defected thick ZnO nanoflakes typically obtained by bottom-up chemical synthesis routes.[30] Secondly, our exfoliation method produces 2D ZnO enriched with two non-polar planes, *viz.* the $(\bar{1}2\bar{1}0)$ *a*-plane and the $(10\bar{1}0)$ *m*-plane (Fig. 1a). Notably, *a*-/*m*-oriented ZnO thin films can overcome the quantum Stark effect,[31] but typically require epitaxial growth, where lattice mismatch with the substrate often induces unwanted interfacial defects and strain. The free-standing *c*-/*a*-/*m*-oriented ZnO obtained from our synthesis can be integrated with any substrate, thus overcoming interfacial constraints associated with film growth. Notably, our exfoliated ultrathin ZnO nanosheets exhibit superior structural quality, being defect free and displaying stable excitons. Our DFT calculations validate the experimentally observed defect-free 2D ZnO by revealing that oxygen defects are less favourable in nanosheets compared with bulk ZnO. The applicability of ZnO nanosheets in 2D optoelectronics is demonstrated through the utilization of ultrathin ZnO nanosheets as the emissive electroluminescent layer in solution-processed hybrid LEDs. This facilitates the integration of 2D ZnO as an active light emitting layer in flexible optoelectronic devices.

RESULTS AND DISCUSSION

Exfoliation of ZnO nanosheets with polar and non-polar orientations

ZnO nanosheets were produced by liquid-phase exfoliation of microparticles in an ethanolic solution of triethylamine (TEA) as detailed in Methods (Fig. 1). SEM and TEM images show that the faceted ZnO microparticles with diameters of 0.5 – 5 μm (Fig. 1b) transform into ZnO nanosheets of hundreds of nm to several μm in lateral dimensions (Fig. 1c). The similarity in lateral dimensions between the parent microparticles and the exfoliated nanosheets highlight the benefit

of our low-sonication-energy-based exfoliation strategy.[32, 33] XPS analysis of the exfoliated nanosheets, along with EDX spectroscopy and elemental x-ray mapping of a representative ZnO nanosheet, reveal signatures corresponding to Zn and O, without any impurities (Fig. S1 and S2). Further examination through the fitted XPS O 1*s* spectrum reveals a significant density of V_O in the exfoliated nanosheets (Fig. S1). Fig. 1d shows the XRD pattern from the ZnO nanosheets drop-cast from the exfoliation suspension, revealing the retention of the wurtzite phase (JCPDS 36-1451) following exfoliation. This is noteworthy as atomically thin ZnO nanosheets grown via bottom-up atomic layer deposition processes often exhibit strong in-plane strain to match the substrate lattice parameters, rather than forming layers with a wurtzite structure.[34] XRD analysis reveals a preferential *c*-plane surface orientation for the exfoliated nanosheets with the (0002) intensity enhanced threefold post-exfoliation, while *a*- and *m*-oriented nanosheets are present in smaller proportions. This result was further confirmed by HRTEM imaging, where a statistical analysis of over 50 nanosheets revealed that approximately half were oriented along the polar (0001) *c*-plane (Fig. 1e), whereas the remaining half exhibited orientation along the non-polar $\{11\bar{2}0\}$ *a*-plane (Fig. 1f) and $\{10\bar{1}0\}$ *m*-plane (Fig. 1g) in similar proportions. This suggests that nVdW ZnO can be exfoliated along the three major low-order crystal planes, with the cleavage along the basal *c*-plane being favorable. This demonstrates a significant advantage of the liquid phase exfoliation method over the conventional bottom-up approach, which typically yields films or nanosheets with only *c*-plane orientation.[35] Notably, the ability to fabricate non-polar *a*- and *m*-plane ZnO layers can eliminate the internal polarization field which is known to reduce efficiencies of ZnO-based optical devices, and such non-polar layers offer a better platform for high-efficiency optoelectronic devices compared with polar *c*-plane.[36]

The HRTEM images of ZnO nanosheets, shown in Fig 1e-g, reveal highly ordered atomic structures, confirming the single crystal nature over lateral distances of several μm. In the case of (0001)-oriented nanosheets, the expected hexagonal lattice structure of ZnO with an interplanar spacing of 0.28 nm in all six directions and a perfect 120° angle between the planes is seen (Fig. 1e). Similarly, the HRTEM image of a ZnO *a*-plane nanosheet reveals two orthogonal interatomic distances of 0.28 nm and 0.52 nm (Fig. 1f), which match closely with the *d*-spacings of the (0001) and $(10\bar{1}0)$ planes of hexagonal ZnO, respectively. For the *m*-plane orientation, the TEM image reveals an interatomic spacing of 0.26 nm, corresponding to the *d*-spacing of the (0001) planes (Fig. 1g). The fast Fourier transform (FFT) patterns, shown in the insets of the corresponding TEM images, further confirm that nanosheets in all orientations are highly crystalline and preserve the wurtzite structure of the parent ZnO.

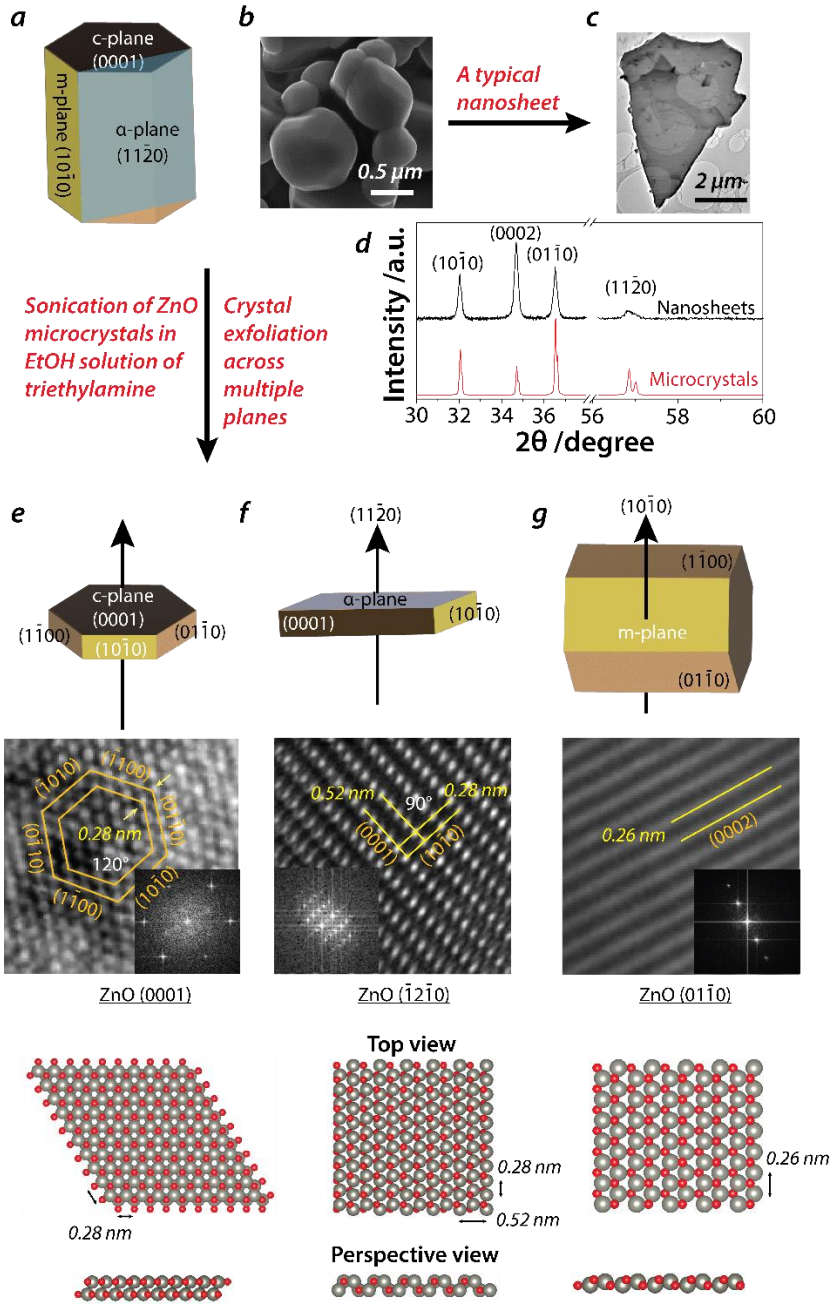

Fig 1. Liquid-phase exfoliation of ZnO microparticles into atomically-thin 2D nanosheets. Schematic depiction of the exfoliation of ZnO microcrystals across three low-index planes of the wurtzite structure presented in **(a)** resulting in highly ordered ZnO nanosheets. The process is illustrated with graphical and atomistic models, showing the atomic arrangement and interatomic distances in the top-most and side planes of the exfoliated nanosheets. Experimental data validates the successful exfoliation of ZnO from **(b)** an SEM image of the parent ZnO microcrystals, **(c)** a TEM image of a typical ZnO nanosheet, **(d)** comparison of the XRD patterns of ZnO microcrystals and nanosheets, and **(e-g)** HRTEM images and FFT patterns of ZnO nanosheets of different orientations revealing highly ordered 2D crystals. Atomistic models (Zn: grey, O: red) for the nanosheets are shown from both top and side views.

Stability of defect-free ZnO nanosheets

Some nanosheets were found to form wrinkles as they dried on the TEM substrate. Fig. 2a shows one such *a*-oriented nanosheet. The robust nature of the high-quality ZnO lattice in the nanosheet is reflected in a highly ordered FFT pattern generated from the entire image. Close inspection of the wrinkled area (Fig. 2b) and the associated line profiles (Fig. 2c) display periodic arrangements of atoms along the $[10\bar{1}0]$ crystal axis. The top of the wrinkle exhibits lattice expansion (*d*-spacing of 0.34 nm in line ii) due to local strain, while the bottom regions of the wrinkle still retain a fully relaxed lattice structure (*d*-spacing of 0.28 nm – the same as the equilibrium value – in lines i and iii). The single-crystalline defect-free nature of ZnO nanosheet is in stark contrast with other 2D materials, which tend to regularly form extended structural defects at the regions of nanosheet folding and wrinkling[32], suggesting that our ultrathin exfoliated ZnO nanosheets have a high level of tolerance for accommodating strain. This observation is supported by our spin unrestricted DFT calculations, which examine the ability of a bent ZnO nanosheet to relax to its unstrained state (Fig. S3). The calculation of the total energy of the system as a function of the amplitude of the sinusoidal ripple imposed on the nanosheet reveals that as while the total energy of the system initially increases with the ripple amplitude; it drops significantly with further increases. This suggests that once a wrinkle is formed on the nanosheet surface, it does not easily restore its unstrained configuration due to the presence of an energy barrier.

To probe the quality of the exfoliated ZnO nanosheets and defect concentrations, we used Raman spectroscopy for isolated nanosheets dispersed on a Si substrate (Fig 2d). Both the parent microparticles and nanosheets display typical Raman modes of wurtzite ZnO, confirming that the wurtzite crystal quality is well preserved during the exfoliation. This structural integrity is further confirmed by the unaltered valence band following exfoliation (Fig. S4). The Raman peaks at 331,

378 and 438 cm^{-1} correspond to intrinsic E_2(high)–E_2(low), A_1(TO) and E_2(high) modes of wurtzite ZnO, respectively. Notably, the E_1(TO) and E_1(LO) peaks at 407 and 582 cm^{-1}, respectively, attributable to V_O defects,[37] are reduced in intensity, indicating a suppression of defects post-exfoliation. The strain-sensitive Raman E_2(high) is located at 437.8 ± 0.5 cm^{-1} for both the ZnO nanosheets and the parent microparticles, indicating that there is no significant induced strain in the nanosheets.

The likelihood of defect formation in ZnO can be quantified by calculating the defect formation energy (E^f) using DFT. We chose to model a 7-monolayer (ML) *c*-plane ZnO nanosheet (Fig. 2e-g), as this orientation is predominantly found in the nanosheet population. For bulk ZnO, we modelled ZnO $(10\bar{1}0)$ *m*-plane surface, as it is the most exposed plane in the parent microparticles (Fig. 2h-j). Interestingly, the DFT calculations reveal that the ZnO *c*-plane nanosheet loses its polarity, unlike the polar (0001) plane in bulk ZnO. This loss of polarity results from the absence of buckling in the ultrathin ZnO (0001) nanosheet, causing it to adopt a flat hexagonal boron nitride (hBN)-type structure, which provides additional stability. The resulting E^f_{Vo} for oxygen vacancies in the ZnO (0001) nanosheet is 4.1 eV, compared with 2.2 eV for the bulk ZnO $(10\bar{1}0)$ system, indicating that the oxygen defect is energetically less favourable in 2D ZnO. Additionally, DFT calculations reveal a significant increase of the calculated bandgap, with E_g = 0.99 and 0.54 eV for the 7-ML (0001) nanosheet and bulk ZnO, respectively (Fig. 2g and j). Although DFT typically underestimates the bandgap, the large difference in the calculated E_g strongly suggests that the bandgap widens as the ZnO nanosheets become atomically thin.

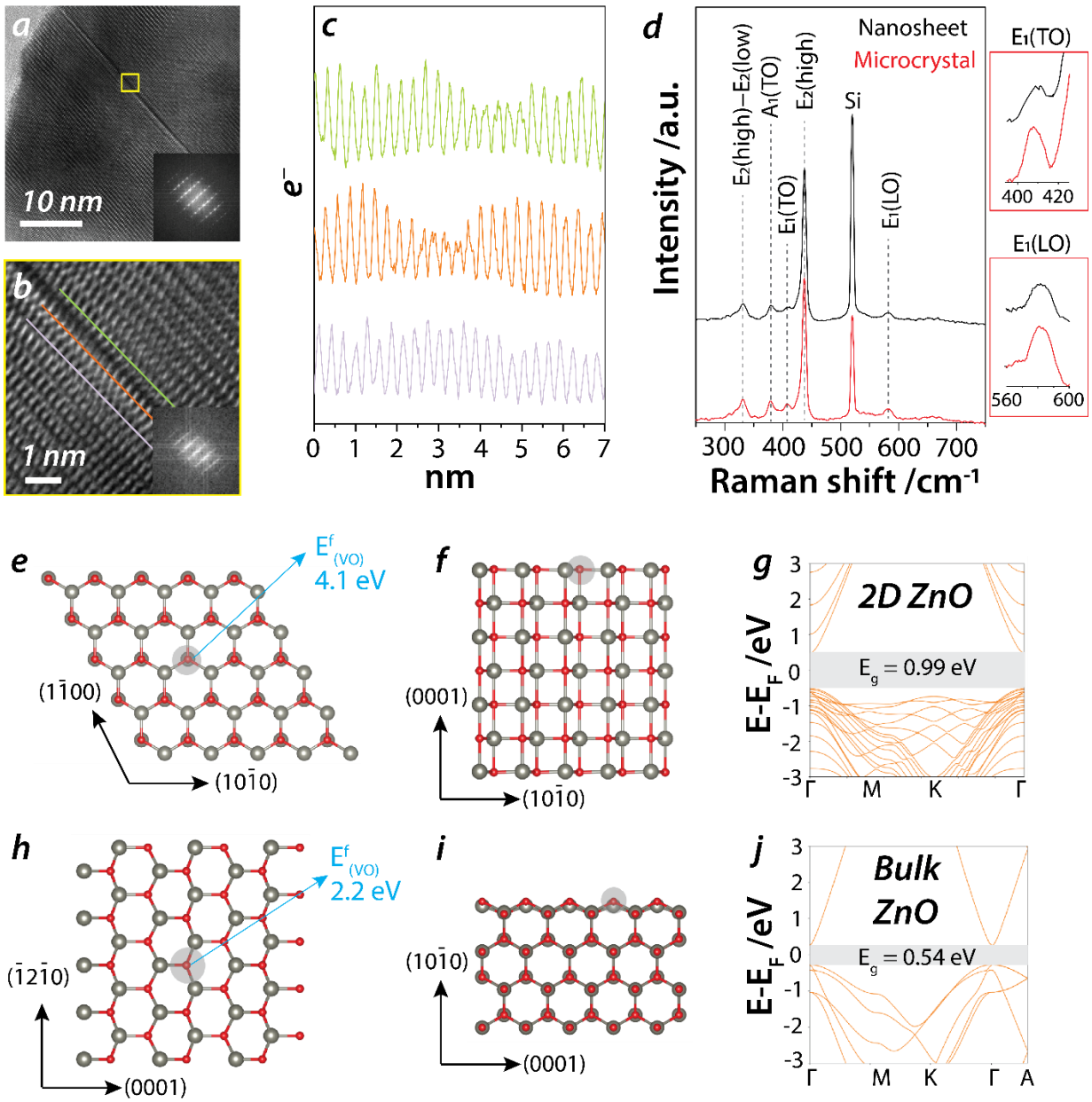

Fig 2. Probing defect-free nature of 2D ZnO nanosheets. (a) HRTEM image of a wrinkled 2D ZnO *a*-plane nanosheet. **(b)** magnified image from the region marked in (a). The FFT patterns from the field of views in (a) and (b) are presented as insets. **(c)** Atomic profile along three lines in the [10$\bar{1}$0] direction marked around and at the wrinkle in (b), supporting long-range crystallinity across the nanosheet surface. **(d)** Raman spectra of ZnO microcrystals and nanosheets, confirming their wurtzite structure and reduction in defect-related Raman modes at 407 and 582 cm^{-1}. **(e-j)** DFT simulations of (e-g) a 7-ML ZnO (0001) plane nanosheet and (h-j) bulk ZnO (10$\bar{1}$0) plane to compare their oxygen vacancy defect formation energies (E^f_{Vo}) and bandgaps (E_g). Panels (e) and (h) show the top views of the surface, (f) and (i) are side views, and the band structures are presented in (g) and (j). The grey circles in (e, f, h, i) indicate the position of the O atom removed for defect formation energy calculations.

Thickness-dependent optical properties of ZnO nanosheet dispersions

To investigate the optical absorbance and photoluminescence (PL) properties of ZnO nanosheets as a function of their thickness, we obtained three size-selected nanosheet fractions using *g*-forces of 500, 5000 and 18000 *g*. These incremental centrifugation steps allow nanosheets to be isolated in different thickness ranges (see Methods). AFM imaging of nanosheets on a mica substrate reveals that nanosheets with large μm-size lateral dimensions could be obtained even at 18000 *g* centrifugation (Fig. 3a-c and see Fig. S5 for TEM and additional AFM images). As expected, ZnO nanosheets obtained at a low centrifugation speed (500 *g*) are generally thicker and larger, with a thickness typically less than 25 monolayers (MLs). Thicker nanosheets are progressively eliminated with increasing *g*-force, resulting in a suspension composed of nanosheets with thicknesses less than 10 MLs at 5000 *g*, while those obtained at 18000 *g* are atomically thin with thicknesses of 2-5 MLs.

We next characterized the optical properties of the size-selected nanosheet suspensions. Fig 3d-f compares the extinction (ε), absorption (α), and scattering (σ) coefficients of nanosheets of different thicknesses normalized to the concentration of ZnO particles dispersed in each suspension (see Fig. S6 and S7 for additional analysis of the optical data). The ultrathin nanosheets from the 18000 *g* centrifugation exhibit over 60 times higher UV absorption capacity (α) than thicker nanosheets from 500 *g* suspensions, which behave similarly to bulk ZnO crystals. This indicates the potential of ultrathin 2D ZnO to serve as an extremely effective UV filter or ultrasensitive photodetector compared with their bulk ZnO counterparts. Additionally, the ultrathin nanosheets resulting from the 18000 *g* centrifugation display extremely high light scattering in the UV region, which progressively decreases with increasing nanosheet thickness. This observation

aligns with recent findings for nanosheets of other wide-bandgap semiconductors that show highly efficient light scattering from high-aspect ratio nanosheets in the non-resonant regime.[38]

Optical absorption edge analysis of the size-selected nanosheet suspensions using the Tauc method yielded a direct optical bandgap (E_g) of 4.1 eV for ZnO nanosheets obtained at the 5000 and 18000 *g*-forces, compared with 3.2 eV for thicker nanosheets obtained at 500 *g* (Fig. S7). The measured bandgap of ultrathin nanosheets in alcohol suspensions is significantly greater than the transition energy at the Γ-point in the Brillouin zone for bulk ZnO. This observation is consistent with Eq. 1 (see next section), which accounts for quantum confinement effects. Moreover, these effects can be further influenced by the presence of OH surface groups that have been reported to effect the band structure in ZnO nanodots.[39, 40] While the origin of this anomalous increase in bandgap is not clear, our experimental observations are supported by DFT calculations (Fig. 2g and j). It is also noted that significant widening of the optical bandgap, up to 1 eV, has been observed in other atomically-thin 2D materials after exfoliation.[32]

Fig. 3g-i shows the PL characteristics of size-selected nanosheet fractions. The PL spectra exhibit two emission bands: the first peak at 3.27 eV (379 nm) corresponds to the near-band-edge UV emission associated with excitonic recombination, and the second much broader peak at 2.5 eV (495 nm) can be ascribed to V_O defects.[20] Thick nanosheets, obtained at a low centrifugation speed of 500 *g*, exhibit a dominant defect emission due to a higher concentration of V_O defects, resembling the bulk state of ZnO. On the other hand, thin nanosheets obtained at higher centrifugation speeds (5000 and 18000 *g*) predominantly exhibit the excitonic emission, with the defect emission intensity decreasing dramatically by over 50 times for the ultrathin nanosheets obtained at 18000 *g* (Fig. 3i and Fig. S8). Furthermore, since the concentration of ZnO nanosheets is the same in each suspension, the observed PL response reveals that, compared with thicker

nanosheets, the ultrathin ZnO nanosheets exhibit considerably enhanced excitonic emission. The defect-free nature of ultrathin ZnO nanosheets is also evident from the transmission cathodoluminescence (CL) spectra collected from isolated nanosheets in Fig. S9, which shows a negligibly weak defect-related emission in an ultrathin nanosheet. The PL and CL observations align with the results from HRTEM, Raman, and DFT results, which collectively confirm that the ultrathin nanosheets are effectively free of point defects. It is noteworthy that in undoped ZnO, n-type conductivity typically arises from impurities such as H, which act as more significant shallow donors than V_O.[41, 42] These inherent electrical properties allow the nanosheets to maintain their viability for the fabrication of optoelectronic devices, as evidenced in the demonstration below.

While the reduction in defects in ultrathin 2D materials during exfoliation has not been reported in either ZnO or any other material, our work suggests that the observed phenomenon in ultrathin 2D ZnO is reminiscent of the inherent strain relaxation and enhanced defect diffusion properties observed in other types of ZnO nanostructures[43]. We consider this as an important finding as liquid-phase exfoliation techniques are currently debated as potentially less viable compared to conventional physical routes for preparing electronic grade 2D materials. Significantly, our results demonstrate that soft liquid-phase exfoliation methods under low-energy sonication conditions can produce superior-quality 2D nanocrystals.[32]

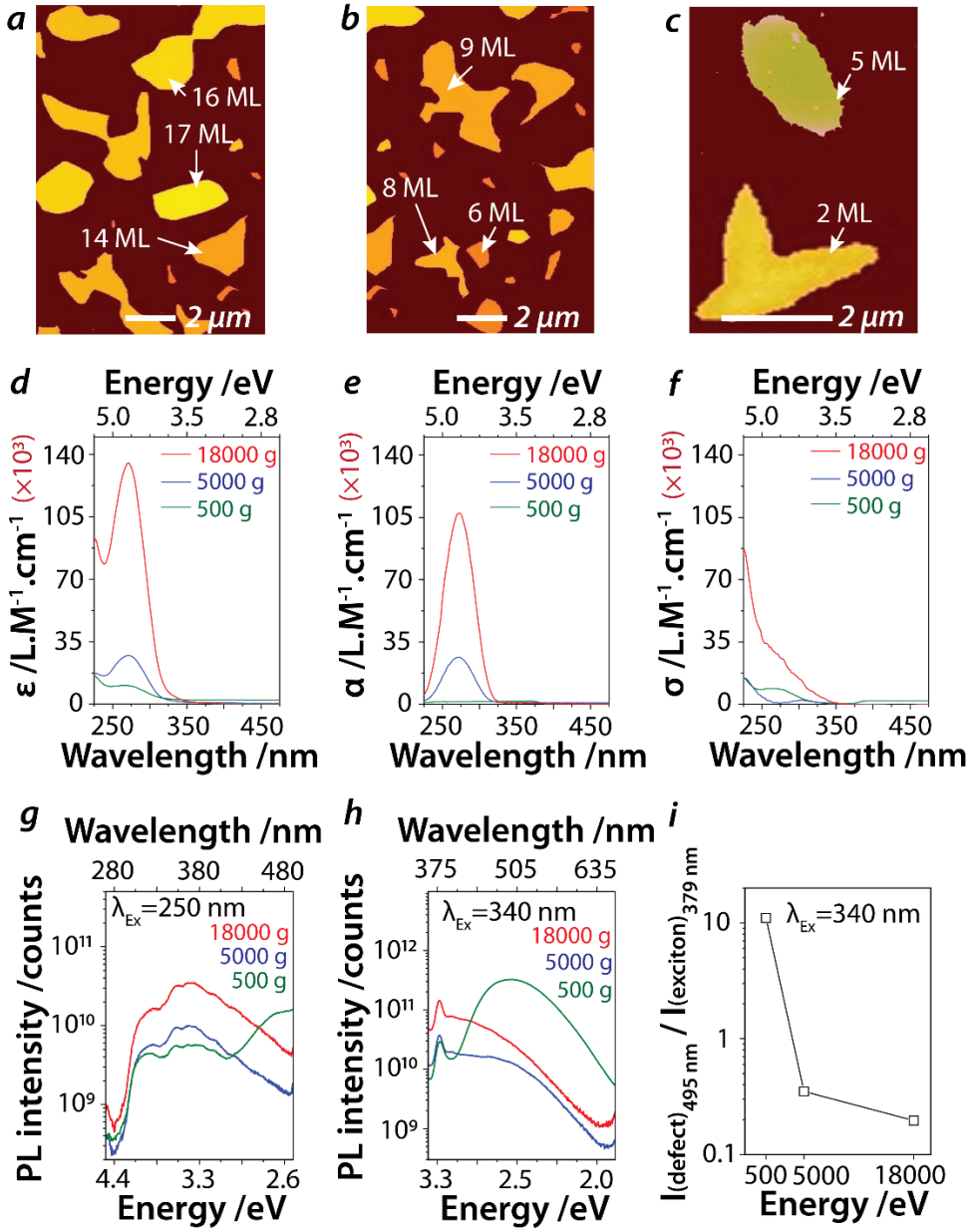

Fig 3. Thickness-dependent optical properties of size-selected ZnO nanosheet dispersions. (a-c) AFM images of ZnO nanosheets obtained at centrifugal forces of 500, 5000 and 18000 *g*, respectively. The exfoliated nanosheets typically have lateral dimensions in the μm range. Increasing the centrifugation speed allows for the isolation of nanosheets with progressively reduced thicknesses, with the thinnest observed nanosheet being 2-ML thick (where one ML is 0.52 nm for a *c*-oriented nanosheet). **(d-f)** Extinction (ε), absorption (α) and scattering (σ) spectra of the nanosheet suspensions. **(g, h)** PL spectra at excitation wavelengths of 250 and 340 nm. The PL spectra show an increase in the excitonic peak at 3.27 eV and suppression of the V_O-related defect emission band at ~ 2.5 eV with an increasing population of thinner ZnO nanosheets obtained with higher *g*-force. These absorbance and PL spectra were acquired from samples with the same concentration of ZnO nanosheets, allowing for direct comparison of their intensities. **(i)** PL intensity ratio $I_{(defect)}/I_{(exciton)}$ as a function of centrifugation speed.

Quantum confinement of excitons in few-atomic-layer thin ZnO nanosheets

To investigate excitons in ultrathin ZnO nanosheets, we used transmission-mode CL with an in-plane spatial resolution of < 10 nm. The CL spectra acquired from individual nanosheets of different thicknesses exhibited a similar spectral shape to those commonly observed in ZnO single crystals[44]. However, we observed a monotonic blue shift and spectral narrowing with decreasing nanosheet thickness (Fig. 4 and Fig. S10). These CL spectra were fitted using the free exciton (FX) peak and its longitudinal optical (LO) phonon side band components by considering the transition probability for phonon-coupled FX-nLO replicas (see Supplementary Note S1). We attribute the FX blue shift to the quantum confinement of free excitons in the ZnO nanosheets and modeled this dependence on the nanosheet thickness, *L*, using a square quantum well potential of infinite height:

$$E_{2D} = E_{bulk} + \Delta E_{2D} = E_{bulk} + \frac{\pi^2 \hbar^2}{2L^2 m_{ex}} \quad (1)$$

where ΔE_{2D} is the exciton energy shift due to the quantum confinement effect, m_{ex} is the reduced effective mass of an exciton, and other parameters have their usual meaning. Using the effective masses, $m_e = 0.23m_0$ and $m_h = 0.59m_0$ for charge carrier transport along the ZnO *c*-plane,[45] we can estimate $m_{ex} = \left(\frac{1}{m_e} + \frac{1}{m_h}\right)^{-1} = 0.165\, m_o$, where m_o is the electron rest mass. Using Eq. (1), a 5 ML thin ZnO nanosheets corresponds to $\Delta E_{2D} = 280 \pm 36$ meV, which is significantly larger than the measured CL peak shift (63 meV). This deviation suggests that the actual confinement of excitons in the exfoliated nanosheets differs from the hard wall potential expected for a perfectly clean ZnO nanosheet, likely due to the interaction of the ZnO surface with chemical species during exfoliation. We further analysed the phonon coupling strength in the nanosheets using the Poisson distribution, $I_n \sim \exp(-S)\frac{S^n}{n!}$, where I_n is the intensity of the *n*th replica and *S* the Huang-Rhys factor[46]. The analysis yields *S* = 0.17 to 0.25 for the nanosheets (Fig. 4c), compared with 0.32 for

bulk ZnO.[46] The weakened coupling strength of excitons to LO phonons for the ultrathin ZnO nanosheets can be attributed to the quantum confinement effect, whereby the exciton wave function becomes less polar, reducing its coupling strength with the polar ZnO lattice via the Fröhlich interaction.[47] The Arrhenius plot of the FX integrated intensity for the 5 ML nanosheet yields a single activation energy of $E_a = 63 \pm 5$ meV (Fig. 4d), comparable to the exciton binding energy in bulk ZnO of 60 meV.[48] This result indicates that the dielectric screening effect on the exciton binding energy due to the medium surrounding the nanosheet is significantly weak, consistent with the small ZnO Bohr radius between 1.8 – 2.4 nm, which is smaller than the nanosheet thickness.

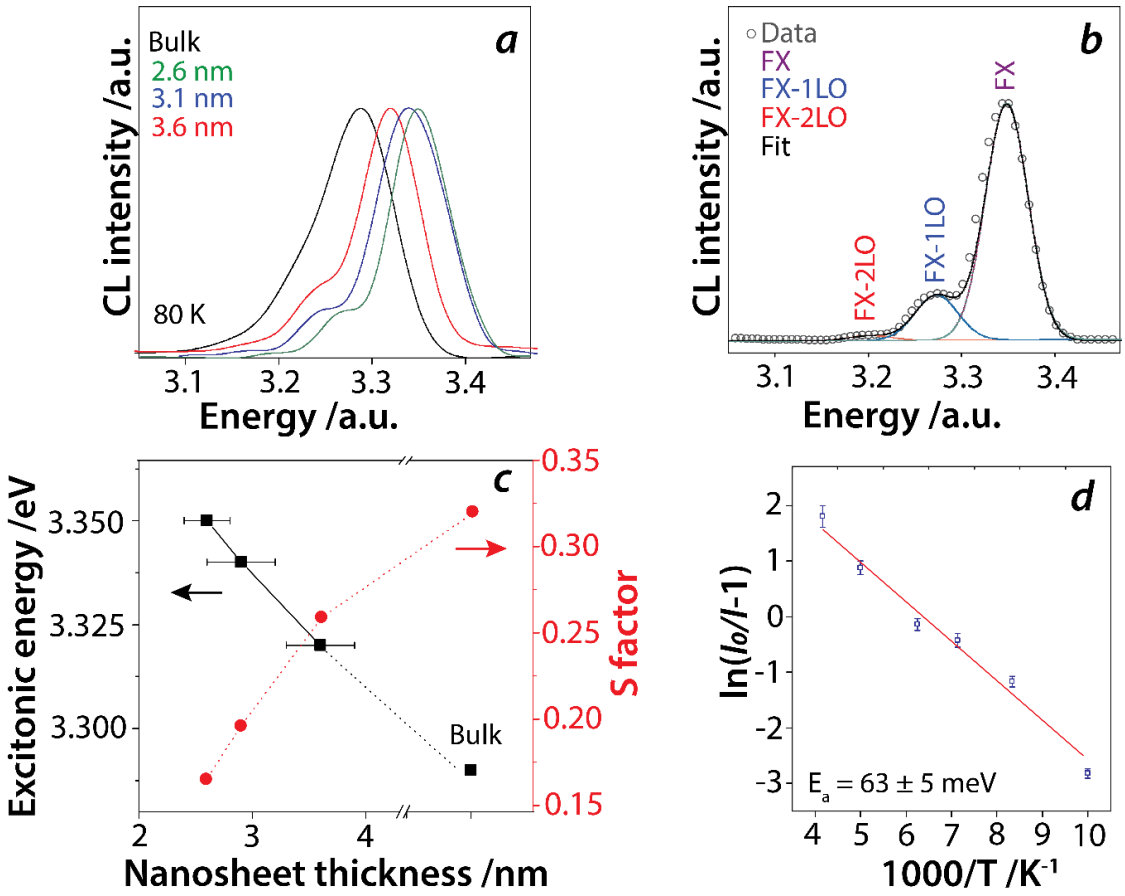

Fig 4. CL analyses of individual ZnO nanosheets. (a) Normalized CL spectra acquired from individual nanosheets and parent ZnO microparticles at 80 K, showing a gradual blue shift of the exciton emission with decreasing nanosheet thickness. **(b)** Fitted CL spectrum showing free exciton (FX) emission and its phonon replicas (FX-1LO and FX-2LO) for a 5 ML nanosheet (t = 2.6 ± 0.2 nm, see the corresponding AFM image in Fig. S10). **(c)** FX energy and Huang-Rhys phonon coupling factor S as a function of nanosheet thickness. **(d)** Arrhenius analysis of the FX integrated intensity yielding E_a = 63 ± 5 meV, corresponding to the exciton binding energy in ultrathin nanosheets.

ZnO nanosheet-based hybrid inorganic-organic LEDs

To explore the utility of 2D ZnO as an active light emitting layer in optoelectronic devices, we fabricated a hybrid inorganic-organic LED with 2D ZnO acting as the emitting layer (EML) via a solution-processed approach (see Methods). We have recently applied this approach to fabricate

flexible OLEDs using 2D carbon dots as the emitter for display devices.[49] The strong UV luminescence of ultrathin ZnO nanosheets was utilized in the LED architecture, which consists of PEDOT:PSS as the hole injection layer (HIL) and a 1,3,5-tris(*N*-phenylbenzimidazol-2-yl)benzene (TPBI) as the electron transporting layer (ETL) to ensure proper alignment of energy levels and efficient charge injection at the interfaces (Fig. 5a).

The TEM image and corresponding EDX maps, obtained from an FIB-milled cross-section of the device verifies the device architecture, revealing a compact ZnO nanosheet layer, approximately 120 nm thick, securely sandwiched between the HIL and ETL layers (Fig. S11). Using the UPS results (Fig. S12) and the energy levels of the HIL and ETL layers,[50] a diagram of energy-band alignment for the multilayer hybrid LED is obtained and depicted in Fig. 5a. The room temperature electroluminescence (EL) spectrum of the LED exhibits a prominent band-edge emission at 3.0 eV (415 nm) along with a shoulder at 2.5 eV (500 nm); the latter emission is attributed to adsorbed chemical species on the surface of nanosheets (Fig. 5b).[51] Each pixel of the LED device exhibits uniform, bright EL emission, which is visible to the eye as intense blue-white light (inset, Fig. 5b). While both the PL and CL data show the defect-free nature of ultrathin ZnO nanosheets, differences in the optical properties of the hybrid LED likely arise from the inorganic-organic interfacial interaction. Specifically, the band-edge EL emission is red shifted compared with the exciton peak of single nanosheets (Fig. 4a) and PL emission from the EML (Fig. S13), this aggregation-induced shift phenomenon is common in thin-film LEDs due to effective energy funneling towards nanosheet aggregates with smaller bandgap.[52] Previous studies have shown that defect-free ZnO nanostructures and thin films are capable of retaining their semiconducting characteristics and exhibit n-type electrical conductivities that enable their successful integration into junction devices.[53, 54] Typical luminance-current-voltage (L-I-V) characteristics of the

nanosheet LED are presented in Fig. 5c, showing that the device can sustain a maximum luminance of 680 cd/m^2 at 9 V and a current density of 340 mA/cm^2. The low turn-on voltage of 3.2 V, compared with blue/cyan hybrid LEDs based on carbon dots,[55] is attributable to carrier tunneling between thin ZnO nanosheets with large contact areas. The maximum luminescence efficiency of 0.35 cd/A is achieved at a current density of 170 mA/cm^2 (Fig. 5d). While solution processable 2D nanosheets of graphene, black phosphorus and metal dichalcogenides have previously been used as a transparent electrode or charge transporting layers in optoelectronic devices[56], the current work marks a significant advancement in achieving a successful realization of a solution-processed 2D material as an active emitter in LEDs. The ability to operate such devices in ambient air highlights the exceptional stability of ultrathin ZnO nanosheets, which possess superior excitonic properties in both ambient and aqueous environments. Since high-efficiency ZnO-based homojunction LEDs have not yet been realized due to *p*-type doping difficulties, our approach for 2D nanosheet-organic hybrid devices could enable high-performance flexible ZnO-based optoelectronic devices.

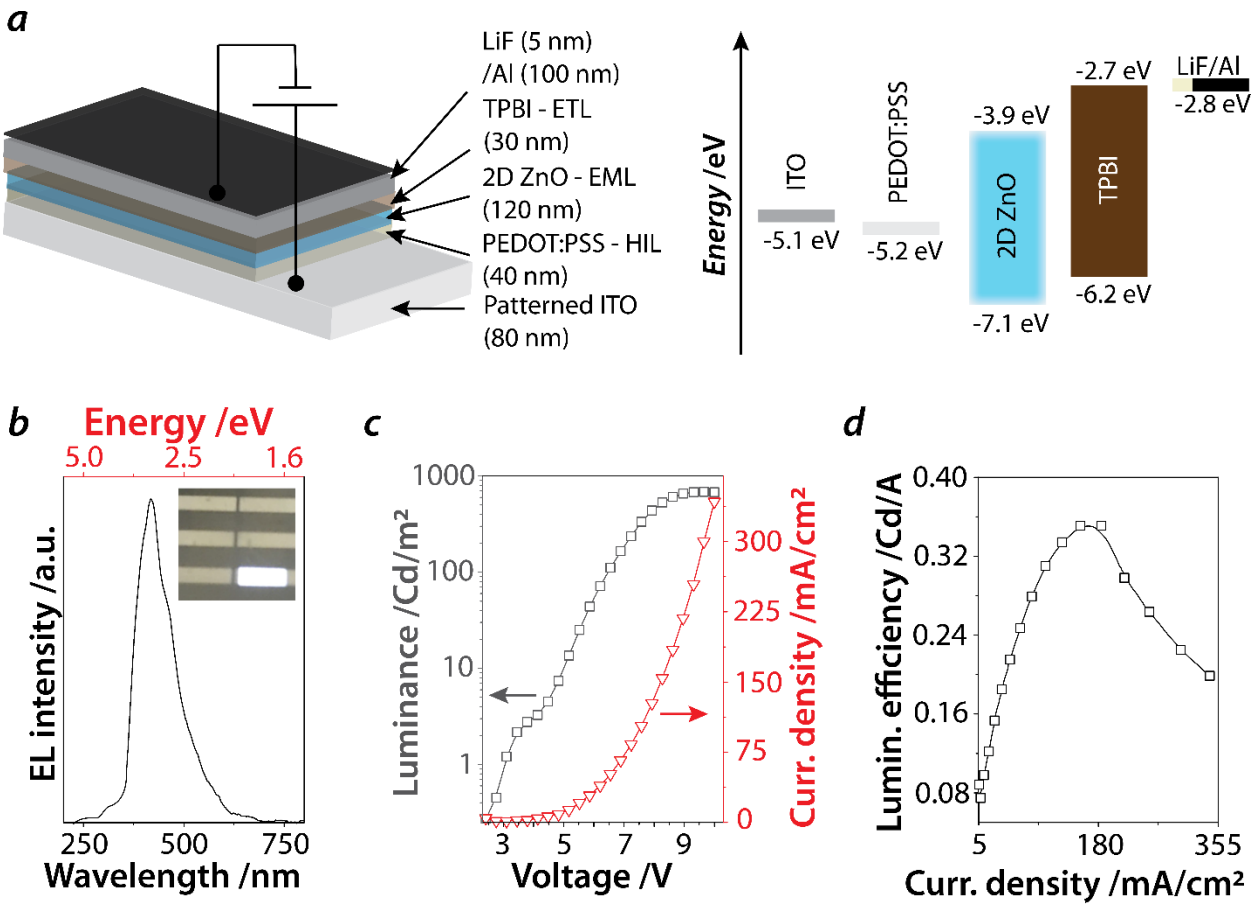

Fig 5. LED device utilizing ZnO nanosheets (a) Device structure of the LED featuring the layer of ZnO nanosheets acts as the emissive EL layer, together with its energy level diagram. The EL emission originates from electrons and holes injected from the TBPI and PEDOT/PSS layers, respectively. **(b)** EL spectrum showing a predominant near-edge emission from the ZnO layer at 3.1 eV. The inset displays six pixels within the device. **(c)** Luminescence-current-voltage characteristics of the LED showing a maximum luminance of 680 cd/m^2. **(d)** Luminescence efficiency plotted against current density, showing a maximum efficiency of 0.35 cd/A achieved at a current density of 170 mA/cm^2.

CONCLUSIONS

Highly crystalline ZnO nanosheets, with thicknesses down to few atomic layers and lateral dimensions in the micrometer range, have been successfully exfoliated along different crystal planes from ZnO microparticles using soft liquid-phase exfoliation. These exfoliated nanosheets

retain the ZnO wurtzite phase and exhibit orientation along both the basal *c*-plane and non-polar *a*- and *m*-planes. Notably, the nanosheets demonstrate exceptional inherent strain relaxation properties, with their lattice parameters matching those of bulk ZnO, resulting in an effective reduction in point defects. Some nanosheets develop wrinkles, which are attributed to unrecoverable strain induced by nanosheet bending, as revealed by first-principles calculations. The ultrathin nanosheets (2-7 monolayers) obtained by high-*g* centrifugation display superior optoelectronic properties, characterized by the absence of defect-related emission and strong excitonic character arising from planar quantum confinement. Our work also represents significant advancements in the fabrication and engineering of solution-processable oxide-based nanosheets for bright LEDs, which could overcome current fabrication limitations of inorganic optoelectronic devices.

METHODS

Production and structural characterization. ZnO nanosheets were obtained by liquid-phase exfoliation of μm-sized ZnO powder in 1% (v/v) ethanolic solution of triethylamine ($N(CH_2CH_3)_3$ - TEA). Previous studies have employed various solvents including dimethyl formamide, n-methyl-pyrrolidone, ethylene glycol, alcohols and water for exfoliating a range of vdW and n-vdW materials.[12] While the exact role of solvents in facilitating the exfoliation of n-vDW materials remains unresolved, effective solvents are expected to passivate dangling bonds at the basal and edge plane intersections during exfoliation, as well as on freshly cleaved reactive surfaces.[12] Additionally, the generation of free radicals and reactive oxygen species (ROS) via sonolysis of the solvent has been observed to contribute to the passivation of these dangling bonds.[57] We have found TEA, as a suitable co-solvent when used in conjunction with water or ethanol, fulfils many criteria for an effective exfoliating solvent for a range of ultrathin 2D crystals.[13, 32, 33] While the precise mechanism of TEA-mediated ZnO exfoliation remains unknown, certain characteristics of TEA offer insights into the exfoliation process. Firstly, as a tertiary amine, TEA possesses an electron lone pair on the nitrogen atom, facilitating strong binding to transition metals, including Zn atoms in the current case. Secondly, the amphiphilicity of TEA molecules enables interaction with both polar and non-polar planes of ZnO. Thirdly, small organic amines and their salts are known for their ability to intercalate in various layered materials.[58] Furthermore, unlike many other types of solvent used for exfoliation, TEA exhibits surfactant-like properties, which can reduce the interfacial tension between ZnO and the solution. Additionally, the highly anisotropic nature of ZnO crystals, characterized by large differences in the surface energy of exposed crystal facets, is also expected to contribute to the facilitation of exfoliation by TEA.

Specifically, 5 mg of ZnO powder was dispersed in 10 mL of the solvent, followed by sonication using a low power ultrasonic bath (Unisonics FXP4M operated at 40 W) for 12 h. The colloidal dispersion obtained from sonication was first centrifuged at 500 *g* force for 5 min to remove any unexfoliated large particles of ZnO and the exfoliated material was harvested from the resultant supernatant. Subsequently, this supernatant was centrifuged separately at different *g*-forces of 500 *g*, 5000 *g* and 18000 *g* for 15 min, which enabled the nanosheets to be size selected into fractions. For microscopic analysis, nanosheet samples were prepared by drop-casting the size-selected dispersions onto a holey carbon-coated Cu grid, mica or a polished silicon substrate and letting the solvent evaporate at room temperature. The morphology of exfoliated nanosheets was characterized using SEM (Zeiss Supra 55VP operated at 10 kV), TEM (JEOL 2100F microscope at 200 kV) and AFM (Veeco Dimension 3100 in tapping mode). XRD analysis was conducted using a Bruker D4 Endeavor diffractometer with the Cu-Kα X-ray source after drop-casting the nanosheets onto a glass substrate. Confocal Raman spectra, collected in backscattering geometry, were acquired using a Horiba LabRAM HR Evolution Raman spectrometer with a 532 nm laser line and excitation power ranging between 0.5 and 50 mW. XPS was conducted on a Thermo Scientific K-Alpha instrument using an Al Kα x-ray source and a low-energy flood gun. XPS measurements were performed on ZnO microparticles and exfoliated nanosheets, which were dispersed on a Si/SiO_2 substrate.

Optical and electronic characterizations. PL spectroscopy was performed on the suspensions of ZnO nanosheets using a Horiba Fluoromax-4 system, while ensuring the same concentration of ZnO in each sample, as determined using inductively coupled plasma – atomic emission spectroscopy (ICP-AES). Optical measurements of ZnO nanosheet suspensions were conducted on a Perkin Elmer Lambda 1050 spectrophotometer equipped with an integrating sphere. The

extinction spectra were acquired in standard configuration, while the absorption component of the extinction was obtained by placing the ZnO suspension within the integrating sphere, allowing for the simultaneous collection of both transmitted and scattered radiation. The extinction spectrum encompasses the contribution of both absorption and scattering components according to the relation $\varepsilon(\lambda) = \alpha(\lambda) + \sigma(\lambda)$. The extinction data for nanosheet suspensions were obtained by transmission (T) data and extinction coefficients calculated using $T = 10^{-\varepsilon C l}$, where ε is the molar extinction coefficient, C the molar concentration of ZnO, and l the cuvette path length. This method was used to assess how the absorption and scattering from nanosheets vary with nanosheet size.

Characterization of the optical properties of individual nanosheets was conducted using transmission-mode CL in an FEI Quanta 200 SEM equipped with an Ocean Optics QEPro spectrometer. In transmission CL mode the spatial resolution of CL is essentially limited by the electron spot size, which is less than 10 nm at the acceleration voltage of 30 kV used in this work. For temperature-resolved CL, ZnO nanosheets from the 18000 *g* dispersion were placed on a TEM grid. All CL spectra were corrected for the overall detection response of the CL spectroscopy system.

Device fabrication and characterization. LEDs based on ZnO nanosheets were fabricated using a pre-patterned ITO glass substrate (from Xianyan Technology). The pre-fabrication step involved washing of the ITO substrate with Alconox and deionized water before sonicating in acetone, ethanol, and isopropanol consecutively for 10 min each. The ITO substrates were then blow-dried with compressed air and treated with UV-plasma for 15 mins. PEDOT:PSS (Heraeus) was filtered with a 0.45 μm PVDF filter and spin coated onto the ITO substrate at 5000 rpm for 30 secs using a spin coater (Laurell Technologies). The spin-coated PEDOT: PSS film was subsequently removed from the contact pads and annealed at 150 °C for 15 min, before being transferred to a

glove box (O_2 < 0.1 ppm, H_2O < 0.1 ppm). Ultrathin ZnO nanosheets obtained at 18000 *g* force were dispersed in toluene (20 mg/ml) and magnetically stirred for 24 h inside a glovebox. A two-step optimized dynamic spin coating condition was used to obtain a uniform layer of ZnO nanosheets over the PEDOT:PSS layer. After the deposition of ZnO nanosheets, the layer was further annealed at 70 °C before being transferred to another glove box fitted with a torpedo thermal evaporator without breaking the vacuum. The following layers were thermally deposited sequentially through a mask at ~10^{-6} mbar pressure: 50 nm of 2,2',2"-(1,3,5-Benzinetriyl)-tris(1-phenyl-1-H-benzimidazole) [TPBi] (Ossila), 5 nm of LiF (Sigma Aldrich), and 100 nm of Ag (Sigma Aldrich). Each substrate consisted of six pixels, each with an area of 10 mm^2 (see Fig 5b). To characterize the device, a lamella cross-section of the device was prepared by using an FEI Scios dualbeam FIB-SEM after applying a thin Pt layer as a protective coating. A substantial stair-step FIB trench was carved on one side of the device, while a rectangular FIB trench was created on the opposite side. Subsequently, the sample was tilted and a section was sliced to release the specimen. The specimen was then progressively thinned using the FIB instrument to achieve electron transparency and transferred onto a Cu TEM grid. HRTEM and EDX imaging were performed in STEM mode using the JEOL 2100F TEM system fitted with a Gatan One View camera and an Oxford X-maxN 80T EDX detector. For high-angle annular dark-field (HAADF) imaging and EDX mapping measurements, an accelerating voltage of 200 kV, a spot size of 2 nm and a camera length of 12 cm were used, while elemental maps were generated using the Oxford AZtec software. Current-Voltage-Luminance (I-V-L) curves of the fabricated LED were recorded using a Keysight B2901A source meter and a Konica Minolta CS-200 luminance meter. EL spectra for the LED active layer were recorded using a Cary Eclipse G9800A spectrophotometer. UPS was performed on a Kratos Axis Supra spectrometer using He I (21.2 eV) as the excitation source.

Theoretical calculations. Density functional theory (DFT) calculations of the 7-ML ZnO (0001) nanosheet and the ZnO bulk terminated with the $(10\bar{1}0)$ surface were performed using the Vienna *Ab initio* Simulation Package (VASP). The exchange-correlation functional in the Perdew-Burke-Ernzerhof (PBE) parametrization was used with the ion-electron interaction described by the projector augmented wave (PAW) method[59]. For all of the calculations, a plane-wave basis set with an energy cutoff of 500 eV was used. For the ZnO bulk unit cell, the lattice parameters and the atomic structure were optimized with a *k*-point mesh of 11 × 11 × 5, yielding the lattice parameters a = 3.288 Å and c = 5.306 Å, which are close to the published values[60]. For the ZnO surface and nanosheet models, the optimization of the atomic structure used a *k*-point mesh of 10 × 10 × 1. For the relaxation of the nanosheet, all atoms were allowed to move freely, while for the ZnO $(10\bar{1}0)$ surface we froze the bottom 2 layers of atoms. The formation energy was calculated using equation (2):

$$E^f = E_{defect} - (E_{pristine} - n_{Zn/O} - \mu_{Zn/O}) \quad (2)$$

where E_{defect} is the total energy of the optimized structure with the vacancy; $n_{Zn/O}$ is the total number of missing Zn and O atoms in the structure; $\mu_{Zn/O}$ is the chemical potential of either the Zn (1.16 eV/atom) or O (4.52 eV/atom); and $E_{pristine}$ is the total energy of the relaxed pristine ZnO structure. For the bent nanosheet, we performed spin-unrestricted DFT calculations with the SIESTA code using the PBE exchange correlation potential[61]. A real-space mesh with a kinetic energy cut-off of 500 Ry was used and the basis functions were radially confined using an energy shift of 0.005 Ry. All atoms in the nanosheet were allowed to relax until the forces on the atoms are less than 0.03 eV/A. A *k*-point mesh of 1 × 1 × 1 was used.

Supporting Information

The Supporting Information is available free of charge at xxx.

Structural, chemical, optical and excitonic analyses of exfoliated ZnO nanosheets, calculations of the properties of bent nanosheets, and the demonstration of the nanosheet-based LED device accompanied by its cross-sectional analysis (PDF)

Correspondence and requests for materials should be addressed to P.S., V.B., or C.T.-T

Author Contributions

V.B., P.S., R.R., M.R.P. and C.T.-T. conceptualized the research and designed the experiments. M.S. synthesized the nanosheets. M.S., M.Z., A.S.P., C.S. and B.J.M. conducted experiments, with all authors contributing to result discussion. S.M. and E.L.H.M. conducted microscopy and cross-sectional characterization of devices. K.T., S.T., M.J.S.S. performed theoretical calculations and modeling.

Acknowledgements

This research was supported under Australian Research Council (ARC) Discovery Projects funding scheme (projects DP210101146 and DP170103477). V.B. thanks the Australian Research Council for funding support through a Future Fellowship (FT140101285). The work was partly undertaken on the Soft X-ray Spectroscopy beamline at the Australian Synchrotron, Australia. Computational resources were provided by the National Computational Infrastructure (NCI, Australia). The following facilities are acknowledged: the Multi-modal Australian ScienceS Imaging and Visualisation Environment (MASSIVE) and the Pawsey Supercomputing Facility.

Competing interests

The authors declare no confliction of interest.

References

1. Lam, D.; Lebedev, D.; Hersam, M. C., Morphotaxy of layered van der Waals materials. *ACS Nano* **2022,** *16* (5), 7144-7167.

2. Akinwande, D.; Huyghebaert, C.; Wang, C.-H.; Serna, M. I.; Goossens, S.; Li, L.-J.; Wong, H.-S. P.; Koppens, F. H., Graphene and two-dimensional materials for silicon technology. *Nature* **2019,** *573* (7775), 507-518.

3. Novoselov, K. S.; Mishchenko, A.; Carvalho, A.; Neto, A. H. C., 2D materials and van der Waals heterostructures. *Science* **2016,** *353* (6298).

4. Balan, A. P.; Radhakrishnan, S.; Woellner, C. F.; Sinha, S. K.; Deng, L. Z.; de los Reyes, C.; Rao, B. M.; Paulose, M.; Neupane, R.; Apte, A.; Kochat, V.; Vajtai, R.; Harutyunyan, A. R.; Chu, C. W.; Costin, G.; Galvao, D. S.; Marti, A. A.; van Aken, P. A.; Varghese, O. K.; Tiwary, C. S.; Iyer, A.; Ajayan, P. M., Exfoliation of a non-van der Waals material from iron ore hematite. *Nat. Nanotechnol.* **2018,** *13* (7), 602-609.

5. Dean, C. R.; Young, A. F.; Meric, I.; Lee, C.; Wang, L.; Sorgenfrei, S.; Watanabe, K.; Taniguchi, T.; Kim, P.; Shepard, K. L.; Hone, J., Boron nitride substrates for high-quality graphene electronics. *Nat. Nanotechnol.* **2010,** *5* (10), 722-726.

6. Tongay, S.; Suh, J.; Ataca, C.; Fan, W.; Luce, A.; Kang, J. S.; Liu, J.; Ko, C.; Raghunathanan, R.; Zhou, J.; Ogletree, F.; Li, J. B.; Grossman, J. C.; Wu, J. Q., Defects activated photoluminescence in two-dimensional semiconductors: interplay between bound, charged, and free excitons. *Sci Rep* **2013,** *3*, 2657.

7. Ma, R. Z.; Sasaki, T., Nanosheets of Oxides and Hydroxides: Ultimate 2D Charge-Bearing Functional Crystallites. *Advanced Materials* **2010,** *22* (45), 5082-5104.

8. Zavabeti, A.; Ou, J. Z.; Carey, B. J.; Syed, N.; Orrell-Trigg, R.; Mayes, E. L. H.; Xu, C. L.; Kavehei, O.; O'Mullane, A. P.; Kaner, R. B.; Kalantar-Zadeh, K.; Daeneke, T., A liquid metal reaction environment for the room-temperature synthesis of atomically thin metal oxides. *Science* **2017,** *358* (6361), 332-335.

9. Jariwala, D.; Sangwan, V. K.; Lauhon, L. J.; Marks, T. J.; Hersam, M. C., Emerging device applications for semiconducting two-dimensional transition metal dichalcogenides. *ACS nano* **2014,** *8* (2), 1102-1120.

10. Walia, S.; Balendhran, S.; Ahmed, T.; Singh, M.; El-Badawi, C.; Brennan, M. D.; Weerathunge, P.; Karim, M. N.; Rahman, F.; Rassell, A.; Duckworth, J.; Ramanathan, R.; Collis, G. E.; Lobo, C. J.; Toth, M.; Kotsakidis, J. C.; Weber, B.; Fuhrer, M.; Dominguez-Vera, J. M.; Spencer, M. J. S.; Aharonovich, I.; Sriram, S.; Bhaskaran, M.; Bansal, V., Ambient Protection of Few-Layer Black Phosphorus via Sequestration of Reactive Oxygen Species. *Advanced Materials* **2017,** *29* (27), 1700152.

11. Kang, J.; Wood, J. D.; Wells, S. A.; Lee, J.-H.; Liu, X.; Chen, K.-S.; Hersam, M. C., Solvent exfoliation of electronic-grade, two-dimensional black phosphorus. *ACS nano* **2015,** *9* (4), 3596-3604.

12. Kaur, H.; Coleman, J. N., Liquid‐Phase Exfoliation of Nonlayered Non‐Van‐Der‐Waals Crystals into Nanoplatelets. *Advanced Materials* **2022,** *34* (35), 2202164.

13. Clarke, C.; Singh, M.; Tawfik, S. A.; Xu, X. X.; Spencer, M. J. S.; Ramanathan, R.; Reineck, P.; Bansal, V.; Ton-That, C., Mono- to few-layer non-van der Waals 2D lanthanide-doped NaYF(4)nanosheets with upconversion luminescence. *2D Mater.* **2021,** *8* (1).

14. Peng, J.; Liu, Y.; Lv, H.; Li, Y.; Lin, Y.; Su, Y.; Wu, J.; Liu, H.; Guo, Y.; Zhuo, Z., Stoichiometric two-dimensional non-van der Waals AgCrS2 with superionic behaviour at room temperature. *Nature Chemistry* **2021,** *13* (12), 1235-1240.

15. Seyler, K. L.; Rivera, P.; Yu, H. Y.; Wilson, N. P.; Ray, E. L.; Mandrus, D. G.; Yan, J. Q.; Yao, W.; Xu, X. D., Signatures of moire-trapped valley excitons in MoSe2/WSe2 heterobilayers. *Nature* **2019,** *567* (7746), 66-+.

16. Lopez-Sanchez, O.; Lembke, D.; Kayci, M.; Radenovic, A.; Kis, A., Ultrasensitive photodetectors based on monolayer MoS2. *Nat. Nanotechnol.* **2013,** *8* (7), 497-501.

17. Georgiou, T.; Jalil, R.; Belle, B. D.; Britnell, L.; Gorbachev, R. V.; Morozov, S. V.; Kim, Y. J.; Gholinia, A.; Haigh, S. J.; Makarovsky, O.; Eaves, L.; Ponomarenko, L. A.; Geim, A. K.; Novoselov, K. S.; Mishchenko, A., Vertical field-effect transistor based on graphene-WS2 heterostructures for flexible and transparent electronics. *Nat. Nanotechnol.* **2013,** *8* (2), 100-103.

18. Gong, C.; Li, L.; Li, Z. L.; Ji, H. W.; Stern, A.; Xia, Y.; Cao, T.; Bao, W.; Wang, C. Z.; Wang, Y. A.; Qiu, Z. Q.; Cava, R. J.; Louie, S. G.; Xia, J.; Zhang, X., Discovery of intrinsic ferromagnetism in two-dimensional van der Waals crystals. *Nature* **2017,** *546* (7657), 265-+.

19. Kim, Y. S.; Park, C. H., Rich Variety of Defects in ZnO via an Attractive Interaction between O Vacancies and Zn Interstitials: Origin of n-Type Doping. *Phys. Rev. Lett.* **2009,** *102* (8), 4.

20. Ton-That, C.; Weston, L.; Phillips, M. R., Characteristics of point defects in the green luminescence from Zn- and O-rich ZnO. *Phys. Rev. B* **2012,** *86*, 115205.

21. Eaton, S. W.; Fu, A.; Wong, A. B.; Ning, C.-Z.; Yang, P., Semiconductor nanowire lasers. *Nat. Rev. Mater.* **2016,** *1*, 16028.

22. Liu, L.; Mei, Z.; Tang, A.; Azarov, A.; Kuznetsov, A.; Xue, Q.-K.; Du, X., Oxygen vacancies: The origin of n-type conductivity in ZnO. *Phys. Rev. B* **2016,** *93* (23), 235305.

23. Børseth, T. M.; Svensson, B.; Kuznetsov, A. Y.; Klason, P.; Zhao, Q.; Willander, M., Identification of oxygen and zinc vacancy optical signals in ZnO. *Applied Physics Letters* **2006,** *89* (26).

24. Knutsen, K. E.; Galeckas, A.; Zubiaga, A.; Tuomisto, F.; Farlow, G. C.; Svensson, B. G.; Kuznetsov, A. Y., Zinc vacancy and oxygen interstitial in ZnO revealed by sequential annealing and electron irradiation. *Phys. Rev. B* **2012,** *86* (12), 121203.

25. Yu, H. H.; Liao, Q. L.; Kang, Z.; Wang, Z. Y.; Liu, B. S.; Zhang, X. K.; Du, J. L.; Ou, Y.; Hong, M. Y.; Xiao, J. N.; Zhang, Z.; Zhang, Y., Atomic-Thin ZnO Sheet for Visible-Blind Ultraviolet Photodetection. *Small* **2020,** *16* (47).

26. Hong, S.; Cho, H.; Kang, B. H.; Park, K.; Akinwande, D.; Kim, H. J.; Kim, S., Neuromorphic active pixel image sensor array for visual memory. *ACS nano* **2021,** *15* (9), 15362-15370.

27. Krishnamurthi, V.; Ahmed, T.; Mohiuddin, M.; Zavabeti, A.; Pillai, N.; McConville, C. F.; Mahmood, N.; Walia, S., A Visible-Blind Photodetector and Artificial Optoelectronic Synapse Using Liquid-Metal Exfoliated ZnO Nanosheets. *Advanced Optical Materials* **2021,** *9* (16).

28. Weigand, C.; Tveit, J.; Ladam, C.; Holmestad, R.; Grepstad, J.; Weman, H., Epitaxial relationships of ZnO nanostructures grown by Au-assisted pulsed laser deposition on c- and a-plane sapphire. *J. Cryst. Growth* **2012,** *355* (1), 52-58.

29. Gulino, A.; Lupo, F.; Fragala, M. E., Substrate-free, self-standing ZnO thin films. *The Journal of Physical Chemistry C* **2008,** *112* (36), 13869-13872.

30. Samanta, P. K.; Saha, A., Wet chemical synthesis of ZnO nanoflakes and photoluminescence. *Optik* **2015,** *126* (23), 3786-3788.

31. Morhain, C.; Bretagnon, T.; Lefebvre, P.; Tang, X.; Valvin, P.; Guillet, T.; Gil, B.; Taliercio, T.; Teisseire-Doninelli, M.; Vinter, B.; Deparis, C., Internal electric field in wurtzite ZnO/Zn0.78Mg0.22O quantum wells. *Phys. Rev. B* **2005,** *72* (24), 241305.

32. Singh, M.; Della Gaspera, E.; Ahmed, T.; Walia, S.; Ramanathan, R.; van Embden, J.; Mayes, E.; Bansal, V., Soft exfoliation of 2D SnO with size-dependent optical properties. *2D Mater.* **2017,** *4* (2), 025110.

33. Ingle, A.; Singh, M.; Tawfik, S. A.; Murdoch, B. J.; Harrop Mayes, E. L.; Sapountzis Spencer, M. J.; Ramanathan, R.; Bansal, V., Reactive Oxygen Species Sequestration Induced Synthesis of β-PbO and Its Polymorphic Transformation to α-PbO at Atomically Thin Regimes. *ACS nano* **2022,** *16* (7), 10679-10691.

34. Hong, H. K.; Jo, J.; Hwang, D.; Lee, J.; Kim, N. Y.; Son, S.; Kirn, J. H.; Jin, M. J.; Jun, Y. C.; Erni, R.; Kwak, S. K.; Yoo, J. W.; Lee, Z., Atomic Scale Study on Growth and Heteroepitaxy of ZnO Monolayer on Graphene. *Nano Letters* **2017,** *17* (1), 120-127.

35. Sohn, J. I.; Hong, W. K.; Lee, S.; Lee, S.; Ku, J.; Park, Y. J.; Hong, J.; Hwang, S.; Park, K. H.; Warner, J. H.; Cha, S.; Kim, J. M., Surface energy-mediated construction of anisotropic semiconductor wires with selective crystallographic polarity. *Sci Rep* **2014,** *4*.

36. Morhain, C.; Bretagnon, T.; Lefebvre, P.; Tang, X.; Valvin, P.; Guillet, T.; Gil, B.; Taliercio, T.; Teisseire-Doninelli, M.; Vinter, B.; Deparis, C., Internal electric field in wurtzite ZnO/Zn0.78Mg0.22O quantum wells. *Phys. Rev. B* **2005,** *72* (24).

37. Zhang, D. F.; Sun, L. D.; Yan, C. H., Optical properties of ZnO nanoplatelets and rectangular cross-sectioned nanowires. *Chemical Physics Letters* **2006,** *422* (1-3), 46-50.

38. Harvey, A.; Backes, C.; Boland, J. B.; He, X. Y.; Griffin, A.; Szydlowska, B.; Gabbett, C.; Donegan, J. F.; Coleman, J. N., Non-resonant light scattering in dispersions of 2D nanosheets. *Nat. Commun.* **2018,** *9*.

39. Jain, G.; Rocks, C.; Maguire, P.; Mariotti, D., One-step synthesis of strongly confined, defect-free and hydroxy-terminated ZnO quantum dots. *Nanotechnology* **2020,** *31* (21), 215707.

40. Bürkle, M.; Lozac'h, M.; McDonald, C.; Mariotti, D.; Matsubara, K.; Švrček, V., Bandgap Engineering in OH‐Functionalized Silicon Nanocrystals: Interplay between Surface Functionalization and Quantum Confinement. *Adv. Funct. Mater.* **2017,** *27* (37), 1701898.

41. Look, D. C.; Farlow, G. C.; Reunchan, P.; Limpijumnong, S.; Zhang, S.; Nordlund, K., Evidence for native-defect donors in n-type ZnO. *Phys. Rev. Lett.* **2005,** *95* (22), 225502.

42. Zhang, S.; Wei, S.-H.; Zunger, A., Intrinsic n-type versus p-type doping asymmetry and the defect physics of ZnO. *Phys. Rev. B* **2001,** *63* (7), 075205.

43. Sun, X. W.; Huang, J. Z.; Wang, J. X.; Xu, Z., A ZnO nanorod inorganic/organic heterostructure light-emitting diode emitting at 342 nm. *Nano Lett.* **2008,** *8*, 1219.

44. Zhu, L. C.; Lem, L. L. C.; Nguyen, T. P.; Fair, K.; Ali, S.; Ford, M. J.; Phillips, M. R.; Ton-That, C., Indirect excitons in hydrogen-doped ZnO. *J. Phys. D-Appl. Phys.* **2017,** *50* (11), 6.

45. Lambrecht, W. R. L.; Rodina, A. V.; Limpijumnong, S.; Segall, B.; Meyer, B. K., Valence-band ordering and magneto-optic exciton fine structure in ZnO. *Phys. Rev. B* **2002,** *65* (7), 12.

46. Wang, L. J.; Giles, N. C., Determination of the ionization energy of nitrogen acceptors in zinc oxide using photoluminescence spectroscopy. *Applied Physics Letters* **2004,** *84* (16), 3049-3051.

47. Yan, B.; Chen, R.; Zhou, W. W.; Zhang, J. X.; Sun, H. D.; Gong, H.; Yu, T., Localized suppression of longitudinal-optical-phonon-exciton coupling in bent ZnO nanowires. *Nanotechnology* **2010,** *21* (44), 6.

48. Meyer, B.; Alves, H.; Hofmann, D.; Kriegseis, W.; Forster, D.; Bertram, F.; Christen, J.; Hoffmann, A.; Stranburg, M.; Dworzak, M., Bound exciton and donor–acceptor pair recombinations in ZnO. *Phys. Status Solidi (b)* **2004,** *241*, 231.

49. Singh, A.; Wolff, A.; Yambem, S. D.; Esmaeili, M.; Riches, J. D.; Shahbazi, M.; Feron, K.; Eftekhari, E.; Ostrikov, K.; Li, Q.; Sonar, P., Biowaste-Derived, Self-Organized Arrays of High-Performance 2D Carbon Emitters for Organic Light-Emitting Diodes. *Advanced Materials* **2020,** *32* (10), 1906176.

50. Yao, K.; Chen, L.; Chen, Y. W.; Li, F.; Wang, P. S., Influence of water-soluble polythiophene as an interfacial layer on the P3HT/PCBM bulk heterojunction organic photovoltaics. *J. Mater. Chem.* **2011,** *21* (36), 13780-13784.

51. Rohr, J. A.; Sa, J.; Konezny, S. J., The role of adsorbates in the green emission and conductivity of zinc oxide. *Commun. Chem.* **2019,** *2*, 52.

52. Ban, M. Y.; Zou, Y. T.; Rivett, J. P. H.; Yang, Y. G.; Thomas, T. H.; Tan, Y. S.; Song, T.; Gao, X. Y.; Credington, D.; Deschler, F.; Sirringhaus, H.; Sun, B. Q., Solution-processed perovskite light emitting diodes with efficiency exceeding 15% through additive-controlled nanostructure tailoring. *Nature Communications* **2018,** *9*, 3892.

53. Ranwa, S.; Kulriya, P. K.; Sahu, V. K.; Kukreja, L.; Kumar, M., Defect-free ZnO nanorods for low temperature hydrogen sensor applications. *Appl. Phys. Lett.* **2014,** *105* (21).

54. Panigrahi, J.; Singh, P.; Gupta, G., Growth and luminescence characteristics of zinc oxide thin films deposited by ALD technique. *J. Lumin.* **2021,** *233*, 117797.

55. Yuan, F. L.; Wang, Z. B.; Li, X. H.; Li, Y. C.; Tan, Z. A.; Fan, L. Z.; Yang, S. H., Bright Multicolor Bandgap Fluorescent Carbon Quantum Dots for Electroluminescent Light-Emitting Diodes. *Advanced Materials* **2017,** *29* (3), 1604436.

56. Ricciardulli, A. G.; Blom, P. W. M., Solution-Processable 2D Materials Applied in Light-Emitting Diodes and Solar Cells. *Advanced Materials Technologies* **2020,** *5* (8), 1900972.

57. Li, Z.; Young, R. J.; Backes, C.; Zhao, W.; Zhang, X.; Zhukov, A. A.; Tillotson, E.; Conlan, A. P.; Ding, F.; Haigh, S. J., Mechanisms of liquid-phase exfoliation for the production of graphene. *ACS nano* **2020,** *14* (9), 10976-10985.

58. Zhou, J.; Lin, Z.; Ren, H.; Duan, X.; Shakir, I.; Huang, Y.; Duan, X., Layered intercalation materials. *Advanced Materials* **2021,** *33* (25), 2004557.

59. Perdew, J. P.; Burke, K.; Ernzerhof, M., Generalized gradient approximation made simple. *Physical Review Letters* **1996,** *77* (18), 3865-3868.

60. Lee, J. H.; Lee, W. J.; Lee, S. H.; Kim, S. M.; Kim, S.; Jang, H. M., Atomic-scale origin of piezoelectricity in wurtzite ZnO. *Physical Chemistry Chemical Physics* **2015,** *17* (12), 7857-7863.

61. Soler, J. M.; Artacho, E.; Gale, J. D.; Garcia, A.; Junquera, J.; Ordejon, P.; Sanchez-Portal, D., The SIESTA method for ab initio order-N materials simulation. *J. Phys.: Condens. Matter* **2002,** *14* (11), 2745-2779.